Electronic Supplementary Material (ESI) for Energy & Environmental Science.
This journal is © The Royal Society of Chemistry 2024

Supporting Information

Mechanical strengthening of perovskite-substrate heterointerface for highly stable solar cells

Xuesong Leng,‡[a] Yichu Zheng,‡[b] Jingjing He,‡[c] Benben Shen,[a] Haonan Wang,[a] Qing Li,[a] Xinyi Liu,[a] Miaoyu Lin,[a] Yifeng Shi,[de] Zhanpeng Wei,[a] Yu Peng,[a] Hua Gui Yang,[a] Qiang Niu,*[c] Shuang Yang*[a] and Yu Hou*[a]

[a] Key Laboratory for Ultrafine Materials of Ministry of Education, Shanghai Engineering Research Center of Hierarchical Nanomaterials, Shanghai Frontiers Science Center of Optogenetic Techniques for Cell Metabolism, School of Materials Science and Engineering, East China University of Science and Technology, Shanghai 200237, China. E-mail: syang@ecust.edu.cn; yhou@ecust.edu.cn

[b] School of Mechatronic Engineering and Automation, Shanghai University, Shanghai 200444, China

[c] National enterprise technology center, Inner Mongolia Erdos Electric Power and Metallurgy Group Company Limited, Ordos 016064, Inner Mongolia, China. E-mail: niuqiang@chinaerdos.com

[d] School of Microelectronics, Shanghai University, Shanghai 201800, China

[e] Laboratory of Thin Film Optics, Shanghai Institute of Optics and Fine Mechanics, Chinese Academy of Sciences, Shanghai, 201800, China

Experimental Section

Materials

N,N-dimethylformamide (DMF, 99%) and chlorobenzene (99.5%) were purchased from Alfa Aesar. Methylammonium iodide (MAI), methylammonium bromide (MABr) and formamidinium iodide (FAI) were purchased from Greatcell Solar Materials. Lead iodide (PbI_2, 99.99%) and lead bromide ($PbBr_2$, 99.9%) were purchased from Energy Chemical. Cesium iodide (CsI, 99.9%) and dimethyl sulfoxide (DMSO, 99.9%) were purchased from Sigma-Aldrich. Ethanol (AR, 99.7%) were purchased from General-Reagent. [6,6]-phenyl-C61-butyric acid methyl ester ($PC_{61}BM$, 99.5%) and bathocuproine (BCP, 99%) were purchased from Nichem chemicals. [2-(9H-carbazol-9-yl)ethyl]phosphonic acid (2-PACz, 98%) were purchased from Tokyo Chemical Industry. Polyhexamethylene guanidine hydrochloride (PHMG, 99%, Mn ~10000-14000) were purchased from Shanghai Macklin Biochemical Technology. Indium-tin oxide (ITO) substrates (8 Ω per square) were purchased from Nippon Sheet Glass.

Device fabrication

Solar cells were fabricated with a p-i-n heterojunction configuration (ITO/2-PACz/perovskite/$PC_{61}BM$/BCP/Ag). Patterned ITO glass substrates were cleaned with soap, water, and ethanol under ultrasonication and then treated with ultraviolet ozone for 30 min. The hole transport layer was prepared by spin-coating 0.3 mg/mL 2-PACz ethanol solution at 3000 rpm for 30 s and then annealed at 100 °C for 10 min. For the hybrid film, PHMG was added into the 2-PACz ethanol solution. The total solid weight of the mixed solution is 0.3 mg/mL, in which there are 0.15 mg of PHMG and

0.15 mg of 2-PACz in 1 mL solution. The processing conditions for PHMG mixed solution are the same as that for pure 2-PACz. After the deposition of perovskite films, 20 mg mL^{-1} $PC_{61}BM$ chlorobenzene and 0.5 mg mL^{-1} BCP ethanol solutions were spin-coated at 2000 rpm for 45 s and 4000 rpm for 45 s, respectively. Finally, 100 nm of Ag was thermally evaporated as the back electrode.

For the triple cation perovskite film, precursor solution was prepared by dissolving CsI, MABr, FAI, $PbBr_2$, and PbI_2 in mixed solvents of DMSO and DMF (v:v = 1:4) with a chemical formula of $Cs_{0.05}FA_{0.81}MA_{0.14}PbI_{2.55}Br_{0.45}$. The perovskite film was prepared by spin-coating at 1000 rpm for 5 s and 4000 rpm for 20 s, and 150 µL chlorobenzene was dropped at 20 s during spinning, followed by annealing at 100 ^oC for 30 min.

For $FAPbI_3$ perovskite film, 1.5 M PbI_2 solution in DMF/DMSO (v:v = 9:1) was spin-coated onto HTL at 1500 rpm for 30 s, and annealed at 70 °C for 1 min prior to cooling to room temperature. Then, a solution of FAI/MACl (90 mg:15 mg in 1 mL IPA) was spin-coated onto the PbI_2 surface at 1800 rpm for 30 s. The perovskite precursor film was then removed from the glove box and thermal annealed at 150 °C for 15 min under a relative humidity of 30-40%.

Characterization

Cross-sectional and surface SEM image of the solar cell device was characterized by field emission scanning electron microscopy (FESEM, HITACHI S4800 and Helions G4 UC). Atomic force microscopy (AFM) (Veeco/DI) was used to obtain the surface morphology and roughness of films. Photoluminescence (PL) spectrum was acquired

by QEPRO spectrophotometer in air at room temperature with the excitation wavelength of 532 nm. PL mapping of perovskite films was measured by a FLRM300 Time-Tech Spectra system. Time-resolved PL (TRPL) spectra were acquired using a Fluorolog-3-p spectrophotometer. Ultraviolet-visible (UV-vis) spectra of the perovskite were carried out on a Cary 500 UV-vis-NIR spectrophotometer. The wettability of perovskite solution on different substrates was measured by Dataphysics OCA20 contact-angle system in ambient atmosphere. Fourier transform infrared spectroscopy (FT-IR) was measured by a Nicolet 6700 spectrophotometer. *J-V* curves of solar cells were measured under an AM 1.5G light simulator (Solar IV-150A, Zolix) calibrated to 100 mW cm^{-2} by a standard KG5-filtered Si reference cell. All devices were measured by a Keithley 2400 digital source meter with a scan rate of 0.15 V s^{-1}. The device active area was masked to be 0.0625 cm^2. Steady state photocurrent output of the best-performing devices was measured by biasing the device at maximum power point. External quantum efficiency (EQE) spectra of PSCs were acquired by Newport-74125 system. Long-term stability of the devices was measured under continuous one-sun illumination in nitrogen by adopting the device structure of ITO/2-PACz/PHMG/perovskite/PC_{61}BM/BCP/Au. Trap density of states (tDOS) of solar cells was derived from the frequency-dependent capacitance (C-f) and voltage-dependent capacitance (C-V), which were performed by an Agilent E4980A LCR meter. Transient photocurrent/photovoltage decays (TPC/TPV) of PSCs were collected on a digital storage oscilloscope (KEYSIGHT, DSOX3104T) with a nitrogen laser (337 nm, SRS NL100). Electrochemical impedance spectra were measured using

an electrochemical workstation (CHI760E) in the frequency range of 1.0 MHz and 1.0 Hz at 0.8 V under dark condition.

Mechanical strength test

For the stress-displacement curve measurements, a double-cantilever beam delamination technique was used on an electronic universal testing machine (LGD-500). The sample specimen adopted a structure of glass/ITO/2-PACz/perovskite/ polyolefin/glass with a lateral size of 1.3 × 1.5 cm^2. Perovskite films with PHMG and without PHMG were prepared on 2-PACz HTL-coated ITO glasses as mentioned above. Then, a 1 × 1 cm^2 polyolefin layer was applied to glue a glass substrate onto the film. The specimen was mounted on the tensile tester fixture, and stretched at an operational rate of 0.5 mm min^{-1} to delaminate the interface. To calculate the specific fracture energy (W), the following equation are used: $W = \int \sigma d\varepsilon$, where σ is the measured stress and ε is the measured strain.[1]

Lifetime analysis of solar cells

We measured the MPP curves at 75, 85, and 95 °C. We present these three sets of MPP curves, as shown in Figure S16a. After aging under 100 mW cm^{-2} illumination and heating at different temperatures for 600 hours, the devices at 75 °C, 85 °C, and 95 °C respectively retained 94.2%, 91.8%, and 86.9% of their initial efficiency.[2,3] We obtain E_a by rearranging the following equation:

$$k\,(T) = Aexp(\frac{-E_a}{k_B T}) \qquad \text{(Eq. 1)}$$

Where k(*T*) is a degradation rate at temperature *T*, A is constant, E_a is the activation energy of degradation, and k_B is Boltzmann's constant. The degradation rate k can be obtained by exponential fitting of the maximum power point (MPP) curve of the perovskite device.

Rearranging Equation 1, the activation energy is equivalent to the slope.

$$E_a = -\frac{\partial ln(k(T))}{\partial(\frac{1}{k_B T})} \quad \text{(Eq. 2)}$$

According to Figure S16b, we obtained Ea of 0.584 ± 0.03 eV, which is the slope of the fitting curve. This thermally activated degradation behavior is similar to the recently reported values of 0.59 eV for $Rb_{0.05}Cs_{0.05}MA_{0.05}FA_{0.85}Pb(I_{0.95}Br_{0.05})_3$,[3] and 0.487 eV for $CsPbI_3$.[2] Therefore, the temperature dependent degradation experiments again demonstrate the excellent stability of the PHMG devices.

Supplementary Note S1.

The model for control and PHMG device numerically solves the system of three coupled equations of Poisson equation, electron and hole continuity equation, and drift-diffusion equation. Poisson's Equation could be written as:

$$\nabla^2\varphi = -\frac{q}{\varepsilon_0\varepsilon_r}\left(p - n + N_D - N_A\right) \tag{S1}$$

where φ is the electrostatic potential, ε_0 is the permittivity of vacuum, ε_r is the relative permittivity, q is the elementary charge, n and p are the electron and hole concentration, and N_D and N_A are the donor and the acceptor concentration. The continuous equations used in this work describe transport, generation, and recombination processes given by

$$\frac{\partial n}{\partial t} = \frac{1}{q}\nabla \cdot J_n + G_n - \mathrm{R_s} - \mathrm{R_t} - \mathrm{R_b} \tag{S2}$$

$$\frac{\partial p}{\partial t} = -\frac{1}{q}\nabla \cdot J_n + G_\mathrm{n} - \mathrm{R_s} - \mathrm{R_t} - \mathrm{R_b} \tag{S3}$$

where G_n and G_p are the carrier generation rate for electrons and holes, R_s, R_t, and R_b represent Shockley-Read-Hall recombination, Auger recombination, and radiative recombination for electrons and holes, respectively. The carrier generation rate could be obtained from

$$G(x) = \int_{\lambda_{\min}}^{\lambda_{\max}} \frac{4\pi k(\lambda)}{\lambda} N_{photo}(\lambda) d\lambda \tag{S4}$$

where λ is the wavelength, $k(\lambda)$ is the extinction coefficient, and N_{photo} is the photon flux at each position. The drift-diffusion equations that describe the behavior of electrons and holes are given by

$$J_n = qn\mu_n(-\nabla\varphi) + qD_n\nabla n \quad \text{(S5)}$$

$$J_p = qp\mu_p(-\nabla\varphi) - qD_p\nabla p \quad \text{(S6)}$$

where the $J_n\,(J_p),\ \mu_n\,(\mu_p),\ and\ D_n\,(D_p)$ are the electron (hole) current densities, electron (hole) mobility, and electron (hole) diffusion coefficients, respectively. The key parameters used for this simulation are listed in Table S1. By solving these equations, the electrical parameters or properties including *JV* curves and distributions of carrier concentration and recombination could be obtained.

Table S1. Comparison of recently reported photovoltaic parameters of PSCs.

PCE (%)	PCE_t/PCE_0	Testing Condition
25.05 (This work)	95.6%	Encapsulated, 1sun illumination, 55 °C, 600 h
23.3 (This work)	97.5%	Encapsulated, 1sun illumination, 55 °C, 1600 h
25.5[4]	98%	N_2, 1 sun illumination, 40 °C, 1000 h
24.5[5]	90%	N_2, 1 sun illumination, 40 °C, 1200 h
25.3[6]	95%	Encapsulated, 1 sun illumination, 65 °C, 1000 h
24.1[7]	94.5%	N_2, 1 sun illumination, 40 °C, 1000 h
24.6[8]	96%	N_2, 1 sun illumination, 25 °C, 1000 h
25.39[9]	96.6%	Encapsulated, 1sun illumination, 1000 h
24.7[10]	90%	N_2, 1 sun illumination, 40 °C, 1000 h
25.5[3]	93%	N_2, 1.2 sun illumination, 25 °C, 5000 h
24.09[11]	85%	Encapsulated, 1 sun illumination, 85 °C, 1560 h

*PCE_t/PCE_0 is the ratio of the device efficiency after and before stability measurements.

Table S2. Key parameters used in the simulation.

Parameter	Unit	Perovskite Control	Perovskite PHMG	PCBM	2-PACZ
Thickness	nm	600		30	5
GB width	nm	2		/	/
Bandgap	eV	1.6		2.4	3.5
Electron affinity	eV	3.9		4.2	2.6
Effective DOS for electrons	cm^{-3}	2×10^{18}		1×10^{20}	1×10^{20}
Effective DOS for holes	cm^{-3}	2×10^{18}		1×10^{20}	1×10^{20}
Doping concentration	cm^{-3}	10^{14}		/	/
Mobility of electrons (holes)	$cm^2 V^{-1} s^{-1}$	1.0 (1.0)		1.0×10^{-2}	(1.5×10^{-4})
Bulk trap density	cm^{-3}	4×10^{15}		/	/
GB interface trap density	cm^{-2}	1×10^{11}		/	/
ETL interface density	cm^{-2}	1×10^{11}		/	/
HTL interface density		1×10^{11}		/	/
Void interface density	cm^{-2}	1×10^{11}	/	/	/
Bimolecular recombination coefficient	$cm^{-3} s^{-1}$	3×10^{-11}		/	/
Auger recombination coefficient	$cm^6 s^{-1}$	1×10^{-28}		/	/
Capture cross section	cm^2	1×10^{-16}			
Thermal velocity	cm^2	1×10^{7}			

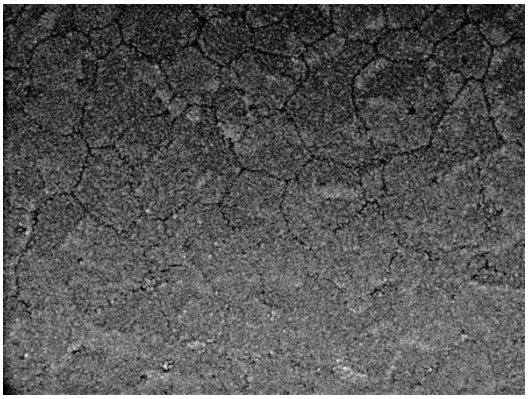

Figure S1. SEM images of the delaminated buried interface of perovskite films based on PHMG substrate.

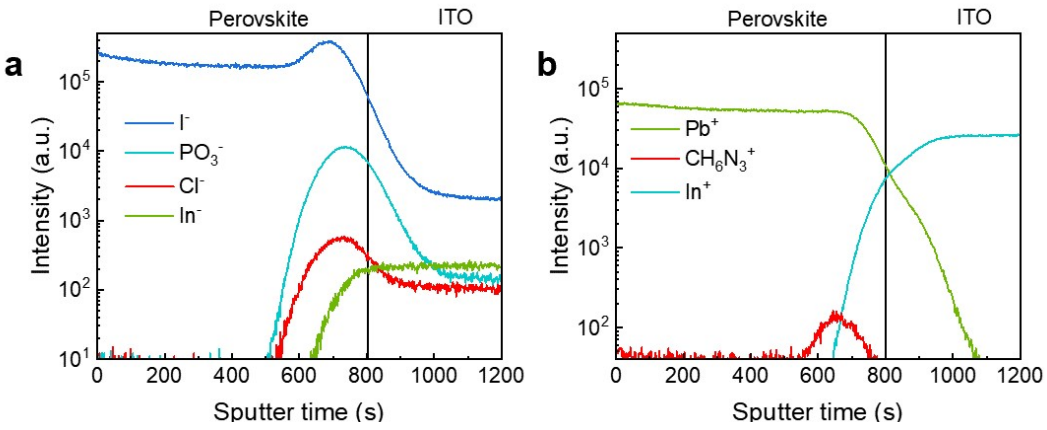

Figure S2. TOF-SIMS analysis of (a) negative and (b) positive ion modes of a typical perovskite device with PHMG interface.

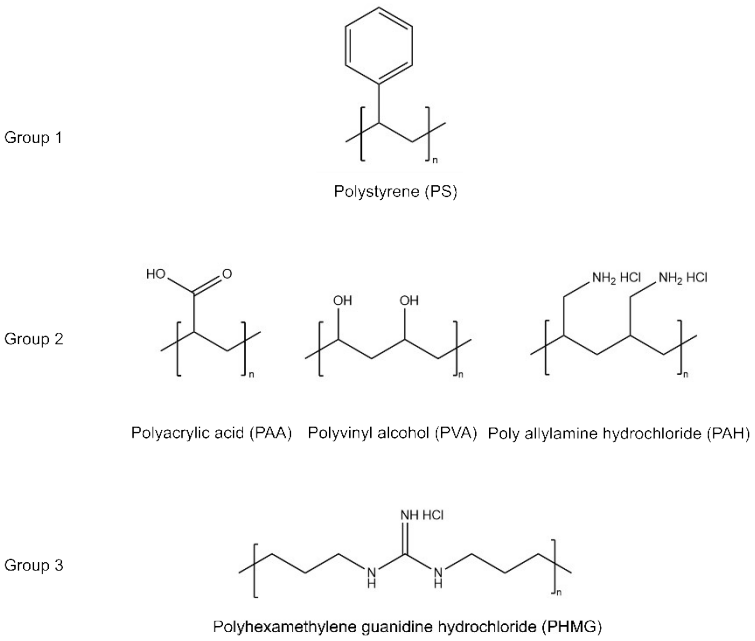

Figure S3. Molecular structure of selected polymer for the mechanical analysis.

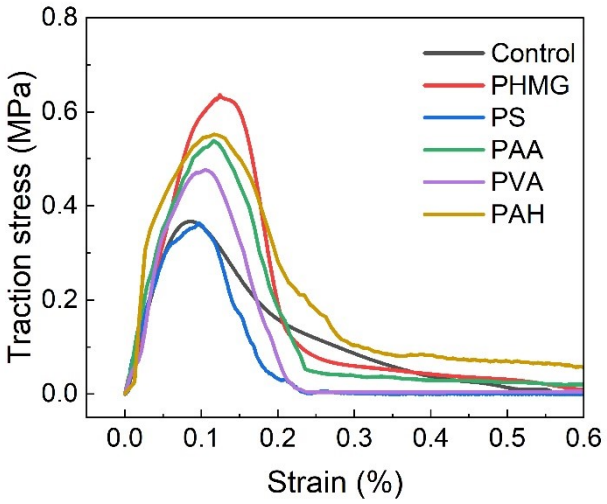

Figure S4. Stress–strain curves of the perovskite device with and without polymeric interface.

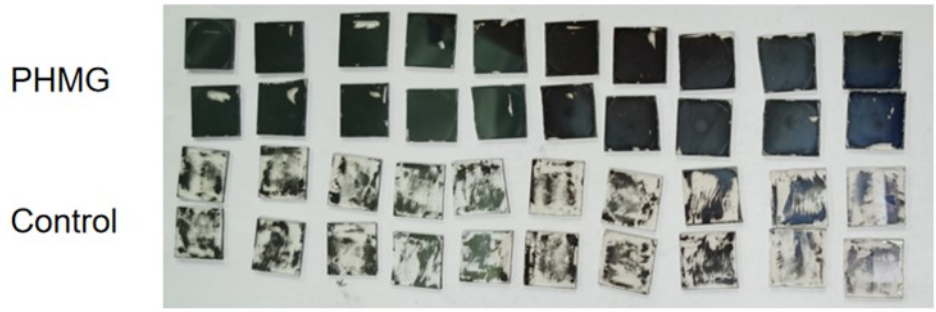

Figure S5. Photographs of delaminated perovskite films of PHMG samples (top two columns) and the control samples (bottom two columns).

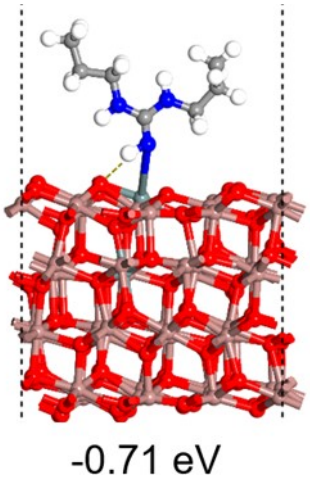

Figure S6. Atomic adsorption model of a PHMG fragment on ITO surface.

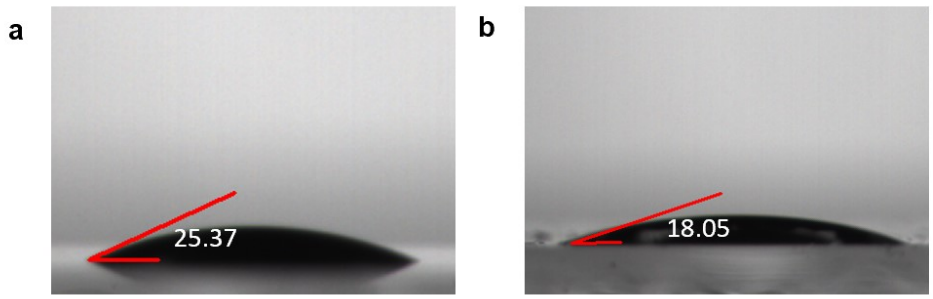

Figure S7. Contact angles of perovskite precursor solution on (a) control and (b) PHMG substrates .

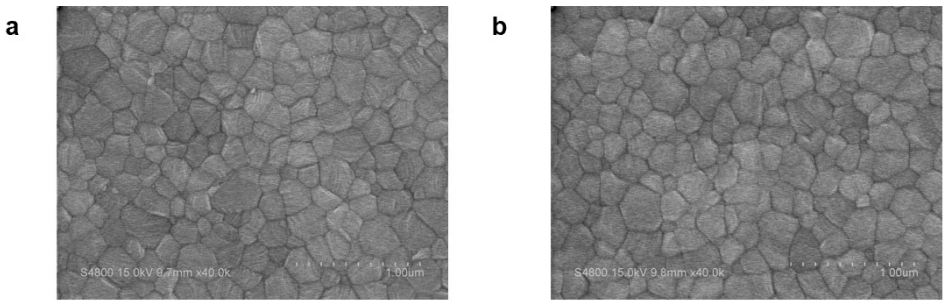

Figure S8. Surface SEM images of perovskite films deposited on (a) control and (b) PHMG substrates.

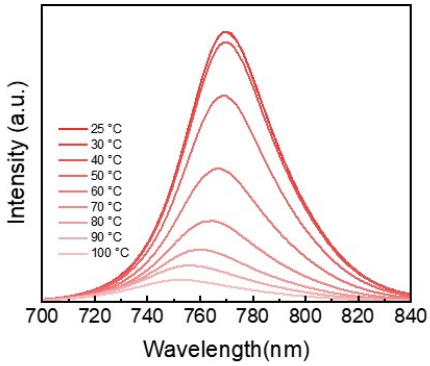

Figure S9. PL spectra of the as-casted perovskite film measured at different temperatures.

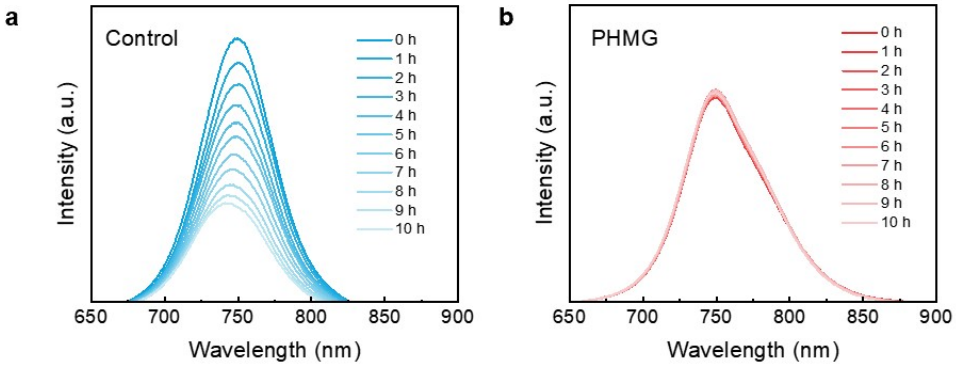

Figure S10. Evolution of steady-state PL signal of perovskite films deposited on (a) control and (b) PHMG substrates.

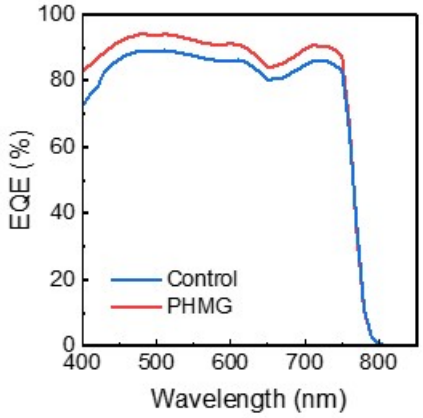

Figure S11. EQE spectra of control and PHMG devices.

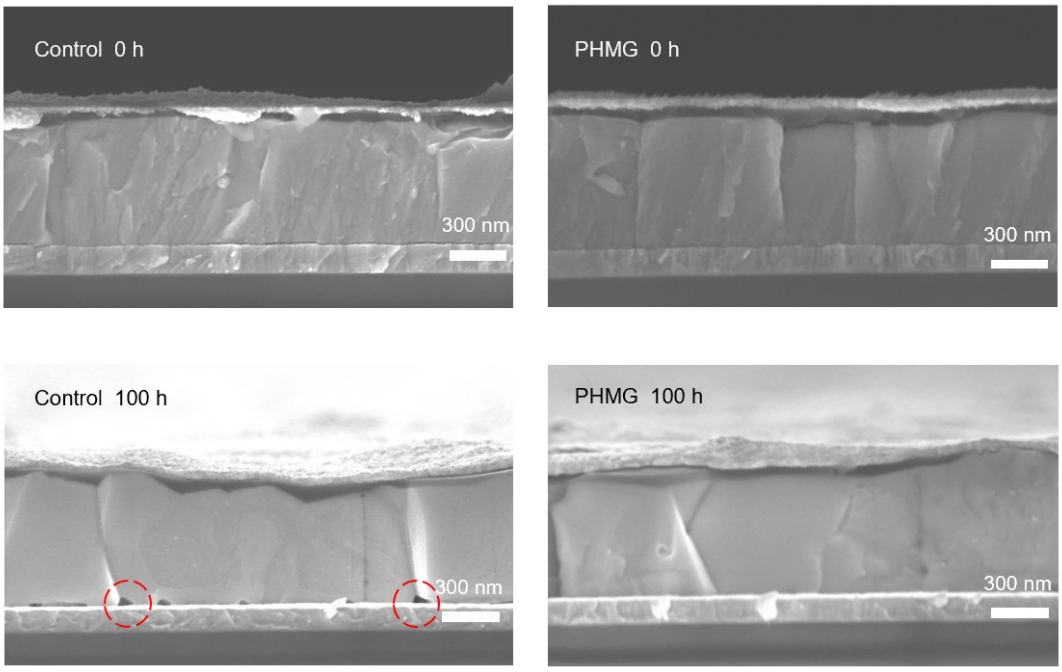

Figure S12. Cross-sectional SEM images of perovskite films with and without PHMG interface prepared by two-step method. The perovskite films were soaked under simulated AM 1.5G irradiation at 55 ^{o}C.

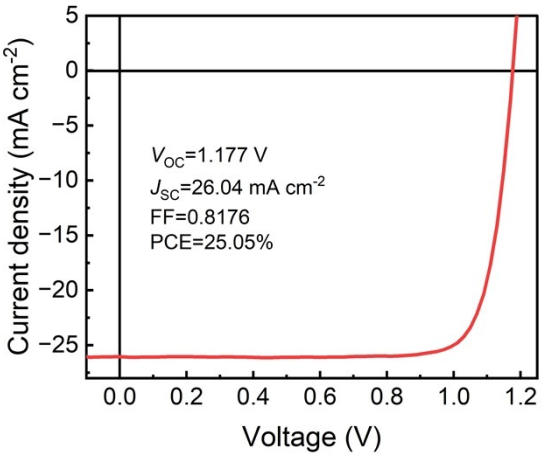

Figure S13. J-V curves of PHMG device based on $FAPbI_3$.

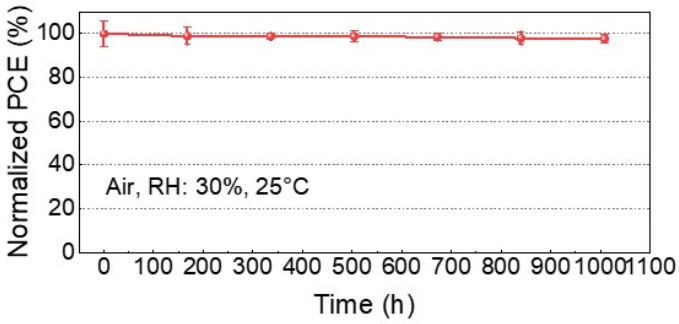

Figure S14. Long-term stability of PHMG device in ambient air.

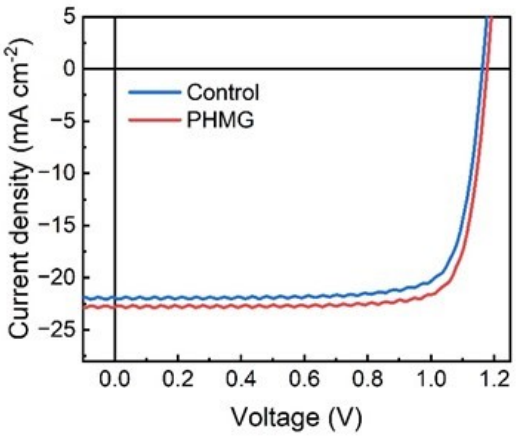

Figure S15. Initial *J-V* curves of control and PHMG devices for the long-term light soaking stability tests.

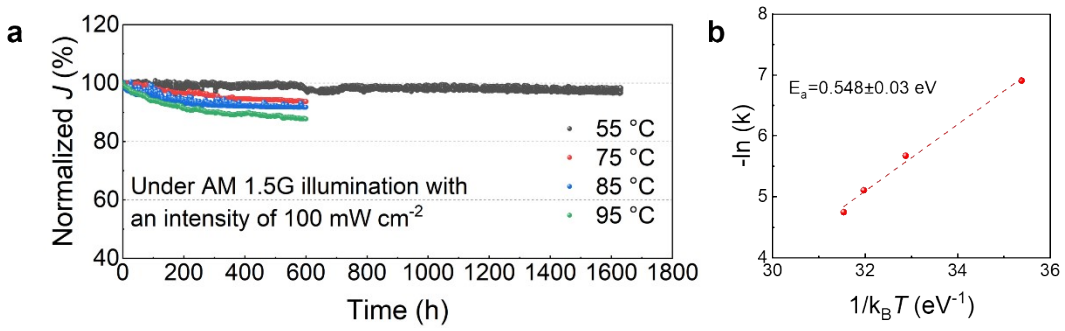

Figure S16. (a) Maximum power point tracking of encapsulated PHMG devices measured under continuous AM 1.5G illumination of 100 mW cm^{-2} at different temperature. (b) The relationship between the natural logarithm of the degradation rate constant and $1/k_BT$, where T is the aging temperature. Linear fitting is used to extract the activation energy (E_a), as indicated by the dashed line.

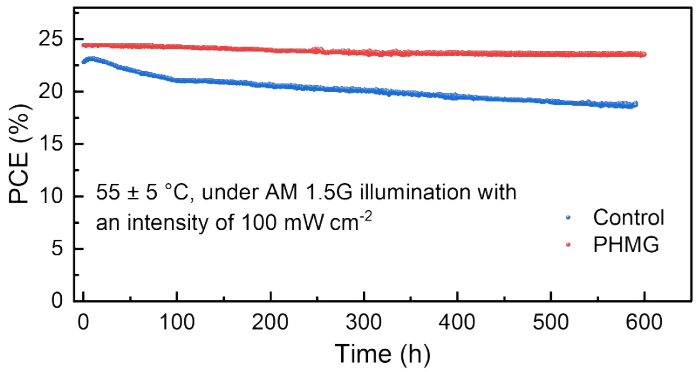

Figure S17. Maximum power point tracking of an encapsulated PHMG device and control device based on void-free $FAPbI_3$ perovskite.

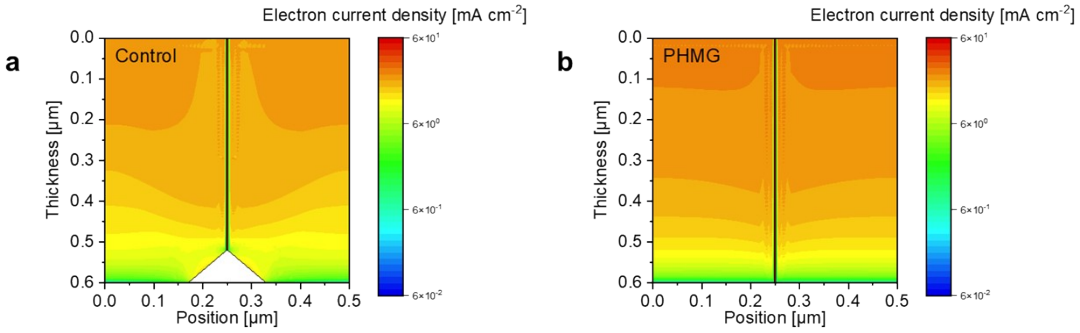

Figure S18. Simulated electron current of (a) control and (b) PHMG devices.

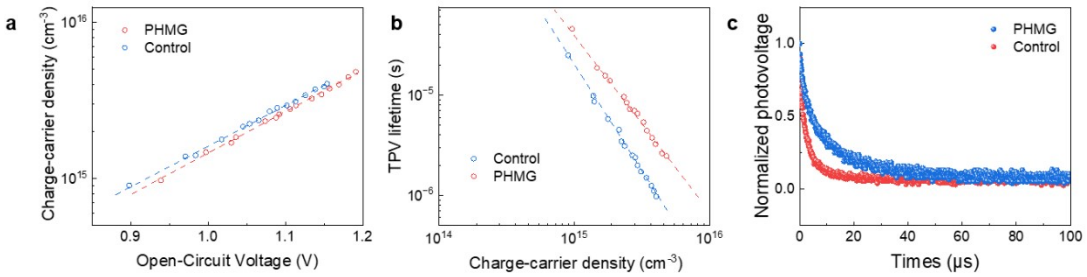

Figure S19. (a) Charge carrier density as a function of V_{OC} of solar cell devices. (b) The relationship between TPV lifetime and charge carrier density of solar cells. (c) TPV decay curves of control and PHMG devices at 1 sun equivalency.

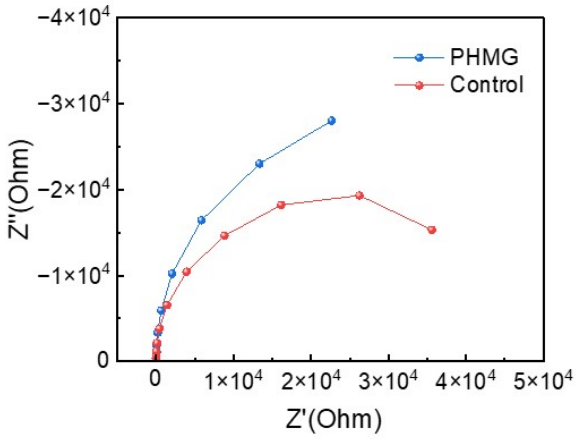

Figure S20. Nyquist plots of control and PHMG solar cell devices recorded at 0.8 V in dark condition.

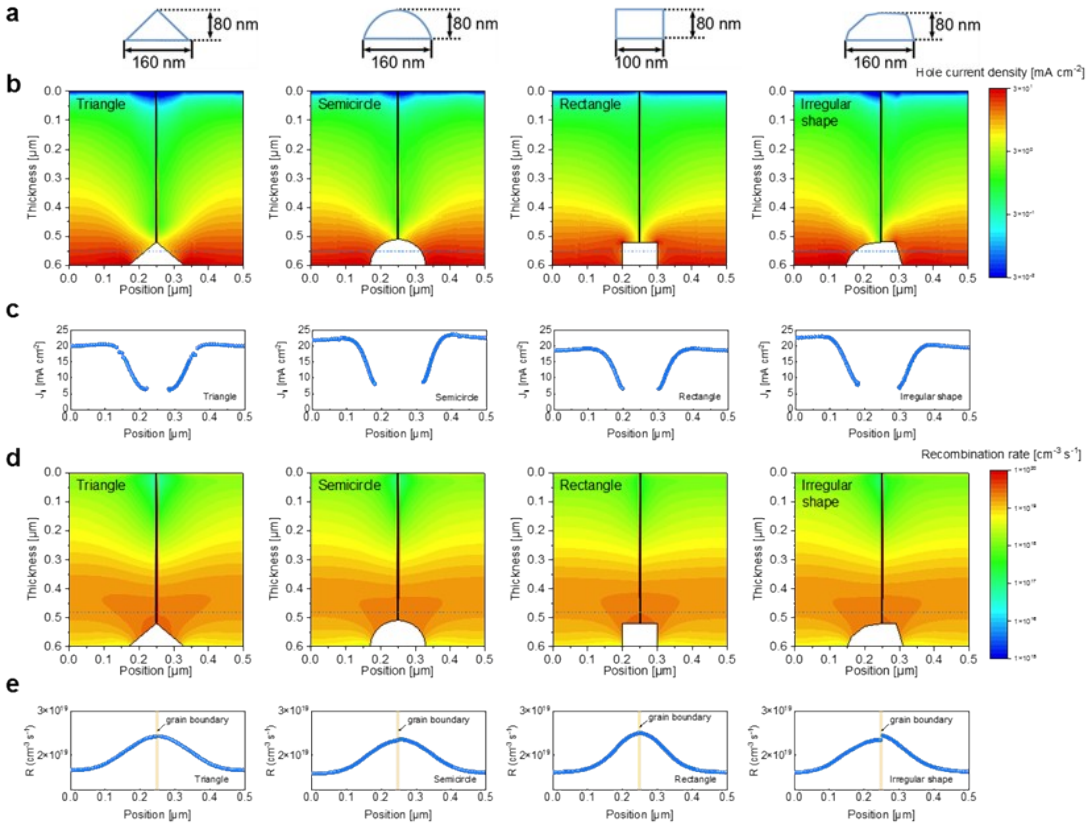

Figure S21. Numerically simulated devices with (a) different shapes of voids and corresponding (b) hole current density distribution, (c) current density extracted from a certain position (blue line in Figure S13a), (d) recombination rate distribution, and (e) recombination rate extracted from a certain position (blue line in Figure S13d).

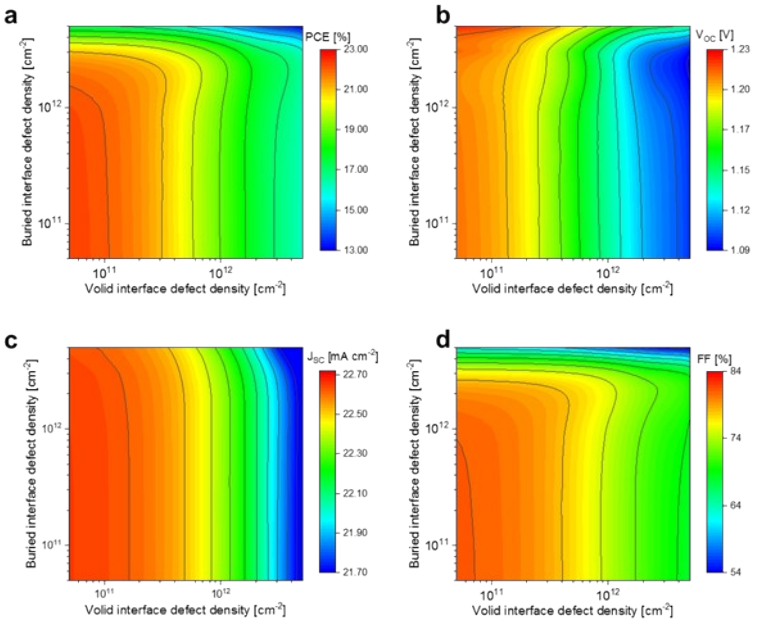

Figure S22. Influence of interfacial defect densities on (a) PCE, (b) V_{OC}, (c) J_{SC}, and (d) FF for device with 80 × 160 nm triangle-shaped void.

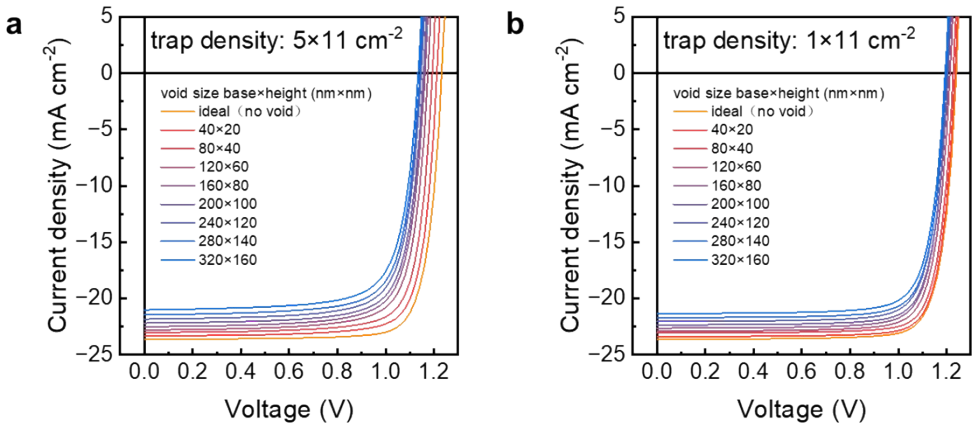

Figure S23. Devices with varied base and height lengths with interface trap density of (a) 5×10^{11} cm^{-2} and (b) 1×10^{11} cm^{-2} for both void and HTL.

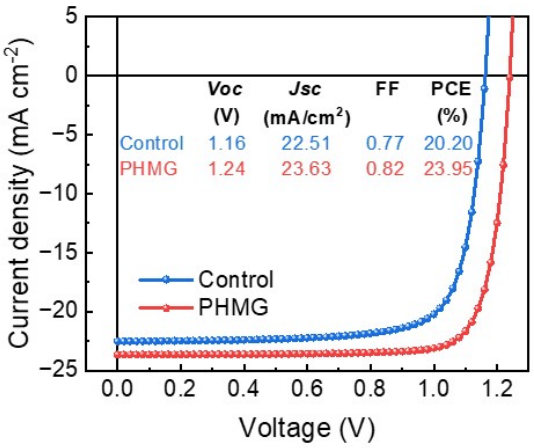

Figure S24. Calculated *J-V* curves of control and PHMG device, respectively.

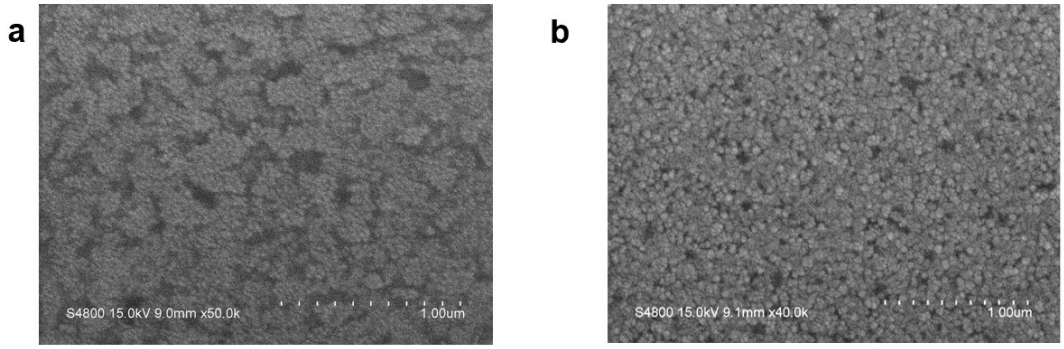

Figure S25. SEM images of (a) control and (b) PHMG substrates.

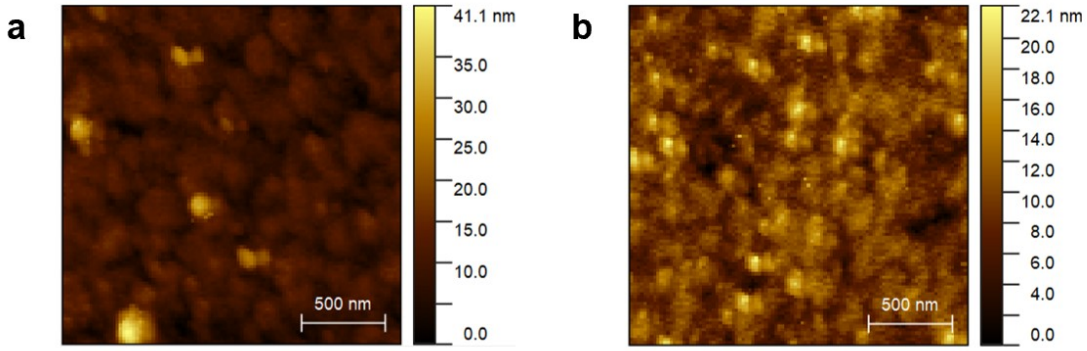

Figure S26. AFM height images of (a) control and (b) PHMG substrates.

Reference

1. M. Hao, T. Duan, Z. Ma, M. G. Ju, J. A. Bennett, T. Liu, P. Guo and Y. Zhou, Adv Mater, 2023, 35, e2211155.
2. X. Zhao, T. Liu, Q. C. Burlingame, T. Liu, R. Holley, G. Cheng, N. Yao, F. Gao and Y.-L. Loo, Science, 2022, 377, 307-310.
3. Q. Jiang, R. Tirawat, R. A. Kerner, E. A. Gaulding, Y. Xian, X. Wang, J. M. Newkirk, Y. Yan, J. J. Berry and K. Zhu, Nature, 2023, 623, 313-318.
4. W. Peng, K. Mao, F. Cai, H. Meng, Z. Zhu, T. Li, S. Yuan, Z. Xu, X. Feng, J. Xu, M. D. McGehee and J. Xu, Science, 2023, 379, 683-690.
5. X. Zheng, Z. Li, Y. Zhang, M. Chen, T. Liu, C. Xiao, D. Gao, J. B. Patel, D. Kuciauskas, A. Magomedov, R. A. Scheidt, X. Wang, S. P. Harvey, Z. Dai, C. Zhang, D. Morales, H. Pruett, B. M. Wieliczka, A. R. Kirmani, N. P. Padture, K. R. Graham, Y. Yan, M. K. Nazeeruddin, M. D. McGehee, Z. Zhu and J. M. Luther, Nature Energy, 2023, 8, 462-472.
6. S. M. Park, M. Wei, N. Lempesis, W. Yu, T. Hossain, L. Agosta, V. Carnevali, H. R. Atapattu, P. Serles, F. T. Eickemeyer, H. Shin, M. Vafaie, D. Choi, K. Darabi, E. D. Jung, Y. Yang, D. B. Kim, S. M. Zakeeruddin, B. Chen, A. Amassian, T. Filleter, M. G. Kanatzidis, K. R. Graham, L. Xiao, U. Rothlisberger, M. Grätzel and E. H. Sargent, Nature, 2023, 624, 289-294.
7. S. Ye, H. Rao, M. Feng, L. Xi, Z. Yen, D. H. L. Seng, Q. Xu, C. Boothroyd, B. Chen, Y. Guo, B. Wang, T. Salim, Q. Zhang, H. He, Y. Wang, X. Xiao, Y. M. Lam and T. C. Sum, Nature Energy, 2023, 8, 284-293.
8. G. Li, Z. Su, L. Canil, D. Hughes, M. H. Aldamasy, J. Dagar, S. Trofimov, L. Wang, W. Zuo, J. J. Jerónimo-Rendon, M. M. Byranvand, C. Wang, R. Zhu, Z. Zhang, F. Yang, G. Nasti, B. Naydenov, W. C. Tsoi, Z. Li, X. Gao, Z. Wang, Y. Jia, E. Unger, M. Saliba, M. Li and A. Abate, Science, 2023, 379, 399-403.
9. Q. Tan, Z. Li, G. Luo, X. Zhang, B. Che, G. Chen, H. Gao, D. He, G. Ma, J. Wang, J. Xiu, H. Yi, T. Chen and Z. He, Nature, 2023, 620, 545-551.
10. F. Zhang, S. Y. Park, C. Yao, H. Lu, S. P. Dunfield, C. Xiao, S. Uličná, X. Zhao, L. Du Hill, X. Chen, X. Wang, L. E. Mundt, K. H. Stone, L. T. Schelhas, G. Teeter, S. Parkin, E. L. Ratcliff, Y.-L. Loo, J. J. Berry, M. C. Beard, Y. Yan, B. W. Larson and K. Zhu, Science, 2022, 375, 71-76.
11. S. M. Park, M. Wei, J. Xu, H. R. Atapattu, F. T. Eickemeyer, K. Darabi, L. Grater, Y. Yang, C. Liu, S. Teale, B. Chen, H. Chen, T. Wang, L. Zeng, A. Maxwell, Z. Wang, K. R. Rao, Z. Cai, S. M. Zakeeruddin, J. T. Pham, C. M. Risko, A. Amassian, M. G. Kanatzidis, K. R. Graham, M. Grätzel and E. H. Sargent, Science, 2023, 381, 209-215.